

Real-time and non-invasive measurements of cell mechanical behaviour with optical coherence phase microscopy

D Gillies^{1,2}, W Gamal², A Downes², Y Reinwald³, Y Yang³, A El Haj³, P O Bagnaninchi^{1*}

¹MRC Scottish Centre for Regenerative Medicine, The University of Edinburgh, Edinburgh, UK

²Institute for Bioengineering, School of Engineering, The University of Edinburgh, Edinburgh, UK

³Institute for Science and Technology in Medicine, Keele University, Keele, UK

*Corresponding Author: Pierre.Bagnaninchi@ed.ac.uk

Abstract

Cell mechanical behaviour is increasingly recognised as a central biophysical parameter in cancer and stem cell research, and methods of investigating their mechanical behaviour are therefore needed.

We have developed a novel qualitative method based on quantitative phase imaging which is capable of investigating cell mechanical behaviour in real-time at cellular resolution using Optical Coherence Phase Microscopy (OCPM), and stimulating the cells non-invasively using hydrostatic pressure. The method was exemplified to distinguish between cells with distinct mechanical properties, and transient change induced by cytochalasin D.

We showed the potential of qualitative phase imaging to detect nanoscale intracellular displacement induced by varying hydrostatic pressure in microfluidic channels, reflecting cell mechanical behaviour. Further physical modelling is required to yield quantitative mechanical properties.

Keywords: optical coherence phase microscopy, mechanical behaviour, real-time monitoring, hydrostatic pressure, phase imaging

1. Introduction

There are more than fifteen cancer deaths per minute globally [1], with over 90% of cancer deaths caused by metastasis [2]. Metastasis is known to alter the mechanical behaviour of cells from the nanoscopic to macroscopic scales [3], with metastatic potential increasing as cell stiffness decreases [4 - 7], and nanoscale features of synthetic surfaces have been shown to influence cell behaviour [8].

Similarly, stem cells are vitally important in regenerative and therapeutic medicine due to their self-renewal and differentiation abilities. Mechanical stimuli have been shown to have a major role in regulating stem cell behaviour, with differentiation controlled by the stiffness of the substrate where stem cells attach, through a mechanosensitive process [9]. Therefore, there is a clear need to investigate the mechanical behaviour of cancer cells and stem cells as well as their response to various mechanical stimuli.

Clinicians have used manual palpation of suspect tissues as a qualitative diagnostic tool for centuries. It is, however, subjective, and carried out on the macroscopic scale. Non-invasive imaging techniques such as ultrasound and Magnetic Resonance Imaging (MRI) elastography have translated to the clinic [10, 11], however both lack the spatial resolution to be used on the cellular scale. The measurement of mechanical behaviour on the nano- and microscopic scale has used techniques such as atomic force microscopy (AFM), optical tweezers, and optical coherence elastography (OCE) [12, 13]. These do,

40 however, suffer from drawbacks for single cell characterisation in that they use contact loading or are
41 unable to assess cellular mechanics in a 3D microenvironment.

42 AFM is one of the most common techniques currently available to assess cell mechanics [14-16]. It
43 uses a cantilever and tip to determine quantitative cell mechanical properties, achieving high
44 resolution and mechanical sensitivity, but is inherently invasive, and as a surface-based technique it
45 cannot investigate intracellular mechanical properties or when cells are cultured in a 3D environment.

46 OCT is a low-coherence interferometry based imaging technique which uses the optical scattering
47 properties of a sample in a manner analogous to ultrasound to create either a 2-D or 3-D image which
48 shows structural features at the micrometer scale [17-19]. OCE is an extension of OCT which maps the
49 mechanical properties of tissue by detecting the depth-resolved deformation produced as a result of
50 compression [13, 20-22]. OCE is comparable to palpation in that a force is applied to the sample under
51 investigation and the resulting displacement tracked [3]. To date, OCE systems typically achieve a
52 depth of focus of 0.5 – 3 mm and A-scan rate greater than 20 kHz [13, 22].

53 Quantitative phase imaging (QPI) is an optical microscopy technique [23, 24] which uses the phase
54 contrast of a sample to improve upon intrinsic contrast imaging. The shift in optical path length (OPL)
55 created by the sample is measured quantitatively at the nanometre scale. It is a powerful label-free
56 tool which has been used to investigate the biophysics of red blood cells [25, 26], cell growth [27], and
57 track microbial motility [28].

58 Combining OCT with high transverse resolution confocal microscopy results in optical coherence
59 microscopy (OCM), achieving sub-micron resolution imaging with high dynamic range and sensitivity,
60 allowing for 3D cellular imaging. OCM further extends to Optical Coherence Phase Microscopy
61 (OCPM), a quantitative phase imaging method, to measure the phase changes and cross-sectional
62 depth information from a sample. It is sensitive to sub-micrometer changes in OPL, and achieves high
63 spatial resolution. It is therefore an ideal candidate for monitoring displacements. OCPM has been
64 used to characterise nanoscale cellular dynamics in live cells [29], and has been shown to measure cell
65 viability based on intracellular optical fluctuations [30, 31].

66 In this study, we aimed to propose a method for the contact-less assessment of cell mechanical
67 behaviour in vitro that will allow further longitudinal studies without damaging the cells or
68 compromising cell culture sterility. Therefore, we described a novel method based on a standard
69 commercial OCT that can measure the relative cell mechanical response to hydrostatic pressure non-
70 invasively and in real-time. This method will be easily translatable to any Fourier-domain OCT and with
71 some modifications to most of the QPI methods.

72

73

74 2. Materials and Methods

75

76 2.1 Cell culture

77 Breast cancer cells (MCF-7) and mouse fibroblasts (3T3) were used in this study to provide two
78 lineages with distinct mechanical properties. Both were cultured in Dulbecco's Modified Eagle
79 Medium (DMEM) with 10% foetal bovine serum, 1% L-glutamine and 1% Penicillin-Streptomycin. Cells
80 were incubated at 37°C and 5% CO₂ and were passaged every 3 days. Cells were dissociated using

81 trypsin-EDTA and transferred to microfluidic channels (microslide IV, Ibidi) 24 hours prior to
82 experimentation. We used adherent cells lines that attached to the bottom substrate of the channels.

83

84 2.2 Hydrostatic Force

85 In this study, we modulated the hydrostatic pressure in microfluidic channels to induce a hydrostatic
86 force on adherent cells attaching at bottom surface of the channels to produce a non-contact force
87 similar to previous work [32]. In this work, we used controlled cyclic square wave pressure, instead of
88 a pressure column. We generated a change in hydrostatic pressure in the microfluidics channels by
89 altering the air pressure in a fluid container (falcon, 50mL), connected through a Tygon (Saint-Gobain,
90 France) tube to microfluidic channels (microslide IV, Ibidi).

91 In first approximation, we can consider the cells as half-spheres attached to an incompressible solid
92 substrate (see figure 1). Pressure and force are transmitted equally to all directions, and on figure 1
93 we will have equal forces on the right and left side of the cell, with no net horizontal hydrostatic
94 component. Whereas there will be a net vertical force, F_v , at the top of the cell proportional to the
95 projected area. For a cell of radius r , we have:

96

$$97 F_v = (\Delta P + \rho gh)(\pi r^2) + \rho g V_w \quad (1)$$

98

99 Where ΔP is the applied pressure change above the atmospheric pressure, ρ is the water density (1000
100 kgm^{-3}), h the height of the water column, and g the gravitational acceleration (9.81 ms^{-2}). V_w is the
101 volume of water on top of the cell starting from the cell top. It can be written as the difference
102 between the cell volume and the volume of an imaginary rectangular box surrounding the cell.

$$103 V_w = 8r^3 - (4/6)\pi r^2 \quad (2)$$

104 Typically for a cell of radius $20 \mu\text{m}$ and $\Delta P=1000 \text{ N.m}^{-2}$ (10 mbar) we calculated a net vertical force of
105 $1.2 \mu\text{N}$. However the actual cross-sectional area of a cell is much lower as attachment to the substrate
106 is made through adhesion focal point. This could lead to acting net vertical force an order of magnitude
107 lower, i.e. in the nano-Newton range.

108 In this study, MCF-7 and 3T3 cells were exposed to cyclic mechanical stimuli in the form of square
109 wave hydrostatic pressure from a microfluidic pressure pump (AF1, Elveflow, France), inside a
110 microfluidic channel with pressure ranging from 1000 Nm^{-2} to 20000 Nm^{-2} with frequencies ranging
111 from 80-300 mHz. It was ensured that no air bubbles were present in the sample medium by allowing
112 a flow of media through the microchannel before sealing with a Luer lock plug (Elveflow, France).

113

114 2.3 Optical coherence phase microscopy

115 *Experimental setup*

116 The OCPM system was based around a commercial Thorlabs Callisto optical coherence tomography
117 (OCT) system, as shown in figure 2. The superluminescent light source was centred at 930 nm with a
118 full width half maximum (FWHM) of 90 nm, with an axial resolution of 5 μm in water. The scanning
119 rate is 1.2KHz; which was order of magnitude lower than state of the art OCT used for OCE. The light
120 source was output to a FC/APC fibre, which is the guided with an F280APC-B collimating lens (Thorlabs,

121 NJ, USA). The light path is then directed by galvanometers which control the image acquisition, and
122 finally is coupled into the side port of a Leica DMIRE2 microscope. The system is built in a common
123 path configuration to improve the phase stability [33]. Using a beamsplitter (Thorlabs, NJ, USA), the
124 brightfield image of the sample was collected digitally using a CMOS camera (Thorlabs, NJ, USA). A full
125 list of components can be found in section 6.

126 The acquired spectra were then processed as described in figure 3. First, the average background was
127 removed, then the signal is resampled in k-space. The modulation of the spectra, collected at a spatial
128 location x_i, y_i , encodes the in-depth location (z_i) of the scattering particles, which are retrieved by zero-
129 padding of the signal and fast Fourier transform. This forms the A-scan at the location (x_i, y_i) and the
130 real part [35] of the complex signal is compressed on a log scale to give a depth-dependent intensity
131 profile; while the phase at each depth z_i of the OCT signal is retrieved from the argument.

132

133 2.4 Quantifying intracellular displacement due to cyclic hydroforce

134 A 4D data cube (256x256x512x96 in x, y, z, t pixels) was captured with an acquisition frequency of
135 1,200 A-scans, or (x, z) scans, per second to sample the varying phase over time. A quantitative
136 measurement of the change in phase was calculated as the differing phase between successive B-
137 scans. A quantitative measurement of the change in phase was calculated as the differing phase
138 between successive B-scans. Therefore, the phase was unwrapped along the time-dimension and
139 not spatially. This was implemented directly with the Matlab (Mathworks) function unwrap.

140 The phase difference was then converted into displacement, d , through the following equation:

$$141 \quad d = \frac{\Delta\Phi\lambda_0}{4\pi n} \quad (3)$$

142 Where; n is the refractive index, λ_0 is the central wavelength and $\Delta\Phi$ is the phase difference between
143 adjacent B scans. In OCPM, the phase stability is defined as the square root of the phase variance,
144 which is inversely related to the SNR [34]. With a theoretical SNR of 83 db in air, the system had a
145 theoretical phase stability of 7×10^{-5} Radians[34]. In liquid medium, the SNR was measured as 35 dB
146 corresponding to a phase resolution of 0.01 radian [34].

147 For rectangular input pressure, the relative displacement of each pixel, Δd , was then determined
148 through the equation:

$$149 \quad \Delta d = 2 * \Delta\Phi \text{RMS}(x, y) \frac{\lambda_0}{4\pi n} \quad (4)$$

150 Where; $\Delta\Phi \text{RMS}(x, y)$ is the root mean squared (RMS) phase change at each pixel as a result of the
151 induced displacement. This gives us a qualitative measurement of the cell mechanical behaviour in
152 response to hydrostatic pressure.

153 Our experimental set-up achieves a scan rate adequate for acquiring the mechanical behaviour of
154 cultured cells. Whilst the scan rate used in our system is lower than the current state of the art, this
155 method is easily translatable to *other systems* where a higher rate could be used.

156 2.5 Assessing whole cell response

157 To assess the whole cell mechanical qualitative behaviour we plotted the distribution of the root
158 mean squared phase for all pixels within the cell, and analysed their distribution. Pixels belonging to
159 a cell were determined by first, manually removing the first strong reflections associated with the
160 plastic substrate, and then using an intensity-based mask to delineate the cells.

161

162 2.5 Cellscale Microsquisher®

163 In order to confirm an appropriate optical phantom for the OCPM set-up, 6% (w/v) agarose beads
164 (Agarose bead technology, Madrid, Spain) of diameter 150 µm to 350 µm were subjected to parallel
165 plate compression in a water bath at a strain rate of 2.5 µms⁻¹ using the Cell Scale Microsquisher® and
166 results recorded in the associated Squisherjoy software. A 1 mm compression plate was attached to a
167 235 µm microbeam. The force vs displacement data was then converted into stress vs strain data, with
168 the associated curve used to obtain a linear regression line from which the elasticity was calculated at
169 10% nominal compression of the sphere.

170 *Theory*

171 Force vs displacement data was converted to stress vs strain using a modified Hertz model [36] as
172 described below.

$$173 \quad \Phi = \cos^{-1}\left(\frac{R-\delta}{R}\right) \quad (5)$$

$$174 \quad a = (R - \delta)\tan\Phi \quad (6)$$

$$175 \quad f(a) = \frac{2(1+\nu)R^2}{(a^2+4R^2)^{3/2}} + \frac{1-\nu^2}{(a^2+4R^2)^{1/2}} \quad (7)$$

$$176 \quad E = \frac{3(1-\nu^2)F}{4\delta a} - \frac{f(a)F}{\pi\delta} \quad (8)$$

177 Where; F is the applied force, R is the sphere radius, δ is the displacement, ν the Poisson's ratio (0.5)
178 and E the Young's Modulus.

179

180 3. Results and Discussion

181 In this paper, we presented an optical coherence elastography method in which the novelty relied
182 mostly on the way the mechanical forces were realised in a non-contact way to allow live cell
183 measurement, and on the associated signal processing techniques. We demonstrated, and
184 exemplified for single pixels in figure 7, that this method created intracellular displacements within
185 the cells that were directly coupled to the input mechanical stimuli, and that they were correlated to
186 transient changes in cell mechanical properties after addition of cytochalasin D, and that they could
187 distinguish two exemplar cell line extensively studied for their mechanical properties. The proposed
188 optical set-up was based on a commercial OCT engine (Callisto, Thorlabs) with relatively low
189 specification when compared to recent advances in the field [], and could therefore translated easily
190 to higher specifications OCT systems and with some small modification to most of the QPI techniques.

191 Figure 5 (a) shows the stress-strain curve of 6% agarose beads (Agarose bead technology, Madrid,
192 Spain) acquired from plate to plate compression tests using the Cell Scale Microsquisher system,
193 shown in (b). This was converted from force-displacement to stress strain using the modified Hertz
194 model described in section 2.5. The mean Young's modulus was determined to be 834 Pa ± 45 Pa at
195 10% nominal compression of the bead. Single beads of varying diameter from 150-350 µm were tested
196 in a water bath. This helped us to confirm that the mechanical properties of agarose beads were in
197 the same order of magnitude as of biological cells that typically range in the 1 kPa region [5]. They
198 were therefore a well calibrated test sample to test the new methods based on OCPM.

199 In figure 6 we report the mean intensity map (a) and phase response (b)-(d) of agarose beads of size
200 150-350 μm , measured using the novel OCPM system. The period of a 100 mbar hydrostatic pressure
201 was varied, with the phase response to 4 s, 6 s, and 12 s cycles shown in figure 6 (b), (c), and (d)
202 respectively at one pixel of the bead. The change in the time varying phase response correlated
203 directly to the change in pressure cycle. This demonstrated that OCPM could monitor nanoscale
204 displacements induced by hydrostatic pressure in materials with mechanical properties comparable
205 to biological cells; and could therefore be used to map the relative mechanical properties of cells in a
206 non-invasive and real-time manner.

207 We then used the OCPM system to measure the mechanical behaviour of MCF-7 cells in response to
208 varying hydrostatic pressure (figure 7), where we plot the response of a single pixel of the cell under
209 test. Here we show a bright field image of the MCF-7 cells in (a) with the corresponding OCPM en-face
210 image and OCPM B-scan or 'cell profile' in figure 7 (b) and (c). Cyclic stress was successfully applied
211 directly to cells within the microfluidic chip and the corresponding displacement was recorded in real-
212 time at the nanometre scale for each pixel of the cell (see figure 7 (d)-(k)). A change in amplitude
213 and/or frequency of the stimuli was translated to a corresponding cell response. In (d), (e) and (f) the
214 amplitude was varied, with the phase response of a single pixel within the cell to 0, 100, and 200mbar
215 cycles of 6s shown respectively. Here we see a clear change in the phase response which is directly
216 proportional to the change in stimulus. Intra-cellular variability gives rise to some variation in the
217 amplitude of the response, however the proportional correspondence of the response cycle to the
218 hydrostatic pressure cycle is clear.

219 In (g), (h) and (i) we show the phase response to a variation in the period of the cyclic stress. The
220 response to 4, 6, and 12s cycles at an amplitude of 200mbar are shown here. Again, we can see that
221 the response clearly correlates to the change in stimulus.

222 We then looked at the ability of the system to monitor the relative biomechanical properties of cells
223 known to be of different stiffness. In (j) we show the phase response of MCF-7 cells to 50mbar of
224 pressure with a 6s period. We then exposed the cells to 10 μM cytochalasin-D, an actin polymerisation
225 inhibitor known to reduce cell stiffness [37], for 180 minutes prior to recording the phase response in
226 (k). We can see an increased response here, indicating that the cells were indeed softer after the
227 addition of Cytochalasin-D. We then calculated the mean RMS of the phase signal in (l) for all pixels of
228 the cell. This gives a quantitative comparison of the relative cell response which confirms that the cells
229 were indeed significantly softer as expected after exposure to the drug ($p < 0.01$), demonstrating the
230 potential of OCPM combined with hydrostatic pressure to monitor non-destructively and in real-time
231 cell mechanical behaviour.

232 In figure 8 we compare two cell lines with distinctly different mechanical properties. We compare the
233 properties of 3T3 cells with MCF-7 cells. 3T3 cells have previously been described as stiffer than MCF-
234 7 in [4]. In (a) we show an en-face image of MCF-7 cells, and of 3T3 in (d). Interferences between the
235 reflections from the cell membrane and the glass surface generates "spatial" coherent interference
236 fringes in intensity when the cell thickness is below the coherence gate ($< 5\mu\text{m}$ in this case), hence the
237 banding effect observed in (d). These fringes were however not detrimental to our method as phase
238 differences were calculated along the time dimension (successive B scans), and not adjacent pixels.
239 We show B-scans, or 'cell profiles' of MCF-7 and 3T3 in (b) and (e) respectively, and the corresponding
240 mechanical contrast maps of relative displacement in (c) and (f), where the relative displacement
241 increases as the map moves to yellow.

242 This map is quantified in (g) and (h) where we plot the relative displacement for all pixels in the cell
243 on a histogram. It is quite clear from this that the mean displacement of the MCF-7 cells is much

244 greater than that of the 3T3, showing a marked difference in the relative displacement between
245 different cell lines. The high level of mean displacement recorded for MCF-7 cells indicates a soft cell,
246 with the low mean displacement if 3T3 indicating a stiffer cell. This data agrees with the figures
247 previously reported in literature, which state that 3T3 cells are stiffer [38, 4].

248 This evidence indicates that this novel non-destructive method is capable of providing a qualitative
249 description of cell mechanical behaviour, and map of mechanical contrast. Qualitative mechanical
250 contrast has been shown as a clinically relevant method in [39-44].

251

252 4. Conclusions

253 We have described a new qualitative method, based on the principles of quantitative phase imaging,
254 to monitor in real-time and non-destructively the mechanical behaviour of cells in monolayers that is
255 directly translatable to the study of the mechanical behaviour of cancer cells and of the stem cell
256 niche. This method is also easily translatable to *in vivo* imaging.

257 We have monitored cell response to cyclic hydrostatic pressure. Nanoscale intracellular displacements
258 were recorded as a function of pressure and can be directly related to the biomechanical properties
259 of cells. Differences were observed in relative strain rates between the cell lines under investigation.
260 Further physical modelling will be required to yield quantitative mechanical properties.

261

262 5 Acknowledgements

263 The authors are grateful to the research group of Dr Anthony Callanan in the Institute for
264 BioEngineering, University of Edinburgh, Edinburgh, UK for facilitating use of the Cell Scale
265 Microsquisher® system.

266 This work was supported by the School of Engineering, University of Edinburgh and the Engineering
267 and Physical Sciences Research Council and Medical Research Council [grant number EP/L016559/1],
268 and the UKRMP Engineering and exploiting the stem cell niche hub [grant number MR/K026666/1].

269 6 Supplier list

270

271 *Hydrostatic Pressure*

Hydrostatic pressure pump	AF1	Elveflow, France
Falcon tube medium accessory kit	50ml	Elveflow, France
Microfluidic channel	Microslide VI	Ibidi, Germany

272

273 *Optical Coherence Phase Microscopy*

OCT system	Callisto	Thorlabs, NJ, USA
Microscope	DMIRE2	Leica, Germany
2D Galvo system, silver coated mirrors	GVS002	Thorlabs, NJ, USA
2D Galvo system linear power supply	GPS011	Thorlabs, NJ, USA
30mm cage compatible smooth bore kinematic mount	KC1	Thorlabs, NJ, USA
F=50mm 1" mounted achromatic doublet, SM1 thread-mount, ARC: 650-1050nm	AC254-050-B-ML	Thorlabs, NJ, USA
30mm Cage cube-mounted non-polarizing beamsplitter, 700-1100nm, M4 Tap	CCM1-BS014/M	Thorlabs, NJ, USA
Fibre collimation package	F280APC-B	Thorlabs, NJ, USA
SM1 threaded adapter	AD11F	Thorlabs, NJ, USA

274

275 *Cellscale Microsquisher*

Micro scale tension compression test system	Microsquisher	Cellscale, ON, Canada
Microbeam cantilever	203.2nm	Cellscale, ON, Canada
Compression plate	1mm x 1mm	Cellscale, ON, Canada

276

277

278 7 References

- 279 [1] B. W. Stewart, C. P. Wild, World cancer report 2014, IARC Press, Lyon, 2014
- 280 [2] C. L. Chaffer, R. A. Weinberg, A perspective on cancer cell metastasis, *Science* 331(6024), 1559-
281 1564(2011)
- 282 [3] B. F. Kennedy, K. M. Kennedy, D. D. Sampson, A Review of Optical Coherence Elastography:
283 Fundamentals, Techniques, and Prospects, *IEEE J. Sel. Topics Quantum Electron.* 20(2), 272-
284 288(2014)
- 285 [4] J. Rother, H. Nöding, I. Mey, A. Janshoff, Atomic force microscopy-based microrheology reveals
286 significant differences in the viscoelastic response between malign and benign cell lines, *Open Biol.*
287 4(5), 140046(2014)
- 288 [5] M. Plodinec, M. Loparic, C. A. Monnier, E. C. Obermann, R. Zanetti-Dallenbach, P. Oertle, J. T.
289 Hyotyla, U. Aebi, M. Bentires-Alj, R. Y. H. Lim, C. Schoenberger, The nanomechanical signature of
290 breast cancer, *Nat. Nanotechnol.* 7(11), 757-756(2012)
- 291 [6] W. Xu, R. Mezencev, B. Kim, L. Wang, J. McDonald, T. Sulchek, Cell stiffness is a biomarker of the
292 metastatic potential of ovarian cancer cells, *PLoS One* 7(10), e46609(2012)
- 293 [7] Z. Zhou, C. Zheng, S. Li, X. Zhou, Z. Liu, Q. He, N. Zhang, A. Ngan, B. Tang, A. Wang, AFM
294 nanoindentation detection of the elastic modulus of tongue squamous carcinoma cells with different
295 metastatic potentials, *Nanomedicine* 9(7), 864-874(2013)
- 296 [8] E. K. F. Kim, E. M. Darling, K. Kulangara, F. Guilak, K. W. Leong, Nanophotography-induced
297 changes in focal adhesions, cytoskeletal organisation, and mechanical properties of human
298 mesenchymal stem cells, *Biomaterials* 31(6), 1299-1306(2010)
- 299 [9] A. J. Engler, S. Sen, H. L. Sweeney, D. E. Discher, Matrix elasticity directs stem cell lineage
300 specification, *Cell* 126(4), 677-89(2006)
- 301 [10] K. J. Glaser, A. Manduca, R. L. Ehman, Review of MR elastography applications and recent
302 developments, *J. Magn. Reson. Imaging* 36(4), 757-774(2012)
- 303 [11] R. M. S. Sigrist, J. Liau, A. E. Kaffas, M. C. Chammas, J. K. Willmann, Ultrasound elastography:
304 review of techniques and clinical applications, *Theranostics* 7(5), 1303-1329(2017)
- 305 [12] B. F. Kennedy, R. A. McLaughlin, K. M. Kennedy, A. C. Chin, A. Tien, B. Latham, C. B. Saunders, D.
306 D. Sampson, Optical coherence micro-elastography: mechanical-contrast imaging of tissue
307 microstructure, *Biomed. Opt. Express* 5(7), 2113-2124(2014)
- 308 [13] B. F. Kennedy, P. Wijesinghe, D. D. Sampson, The emergence of optical elastography in
309 biomedicine, *Nat. Photon* 11, 215-221(2017)
- 310 [14] G. Binnig, C. F. Quate, C. Gerber, Atomic force microscope, *Phys. Rev. Lett.* 56(9), 930-933(1986)
- 311 [15] M. Radmacher, R. W. Tillamnn, M. Fritz, H. E. Gaub, From molecules to cells: imaging soft
312 samples with the atomic force microscope, *Science* 257(5078), 1900-1905(1992)
- 313 [16] D. Tsikritsis, S. Richmond, P. Stewart, A. Elfick, A. Downes, Label-free identification and
314 characterisation of living human primary and secondary tumour cells, *Analyst* 140(15), 5162-
315 5168(2015)

316 [17] D. Huang, E. A. Swanson, C. P. Lin, J. S. Schuman, W. G. Stinson, W. Chang, M. R. Hee, T. Flotte,
317 K. Gregory, C. A. Puliafito, J. G. Fujimoto, Optical Coherence Tomography, *Science* 254(5035), 1178-
318 1181(1991)

319 [18] P. H. Tomlins, R. K. Wang, Theory, developments and applications of optical coherence
320 tomography, *J. Phys. D: Appl. Phys.* 38(15), 2519(2005)

321 [19] A. M. Zysk, F. T. Nguyen, A. L. Oldenburg, D. L. Marks, S. A. Boppart, Optical coherence
322 tomography: a review of clinical development from bench to bedside, *J. Biomed. Opt.* 12(5),
323 051403(2007)

324 [20] J. M. Schmitt, OCT elastography: imaging microscopic deformation and strain of tissue, *Opt.*
325 *Express* 3(6), 199-211(1998)

326 [21] H. Ko, W. Tan, R. Stack, S. A. Boppart, Optical coherence elastography of engineered and
327 developing tissue, *J. Tissue Eng.* 12(1), 63-73(2006)

328 [22] A. Curatolo, M. Villiger, D. Lorenser, P. Wijesinghe, A. Fritz, B. Kennedy, D. D. Sampson,
329 Ultrahigh-resolution optical coherence elastography, *Opt. Lett.* 41(1), 21-21(2016)

330 [23] G. Popescu, Quantitative phase imaging of cells and tissues, McGraw-Hill, New York, 2012

331 [24] M. Mir, B. Bhaduri, R. Wang, R. Zhu, G. Popescu, Quantitative Phase Imaging, *Progress in Optics*
332 57, 133-217(2012)

333 [25] G. Popescu, Y. Park, W. Choi, R. R. Dasari, M. S. Feld, K. Badizadegan, Imaging red blood cell
334 dynamics by quantitative phase microscopy, *Blood Cell Mol. Dis.* 41(1), 10-16(2008)

335 [26] Y. Park, T. Yamauchi, W. Choi, R. Dasari, M. S. Feld, Spectroscopic phase microscopy for
336 quantifying hemoglobin concentrations in intact red blood cells, *Opt. Lett.* 34(23), 3668-3670(2009)

337 [27] K. Park, L. J. Millet, N. Kim, H. Li, X. Jin, G. Popescu, N. R. Aluru, K. J. Hsia, R. Bashir,
338 Measurement of adherent cell mass and growth, *Proc. Natl. Acad. Sci. USA* 107(48), 20691-
339 20696(2010)

340 [28] J. Kühn, B. Niraula, K. Liewer, J. K. Wallace, E. Serabyn, E. Graff, C. Lindensmith, J. Nadeau, A
341 Mach-Zender digital holographic microscope with sub-micrometer resolution for imaging and
342 tracking of marine micro-organisms, *Rev. Sci. Instrum.* 85(12), 123113(2014)

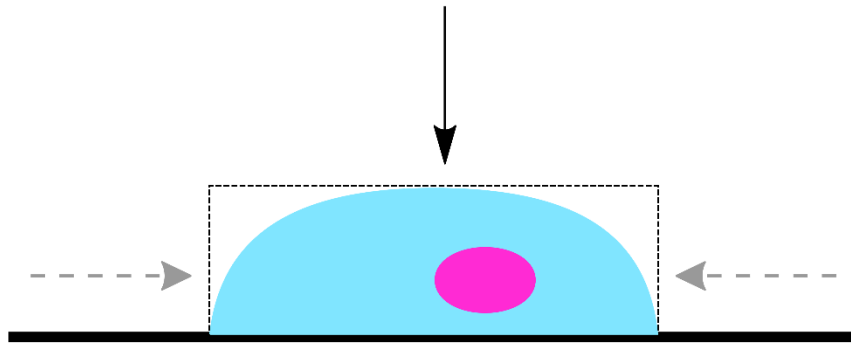
343 [29] A. K. Ellerbee, T. L. Creazzo, J. A. Izatt, Investigating nanoscale cellular dynamic with cross-
344 sectional spectral domain phase microscopy, *Opt. Express* 15(13), 8115-8124(2007)

345 [30] C. Holmes, M. Tabrizian, P. O. Bagnaninchi, Motility imaging via optical coherence phase
346 microscopy enables label-free monitoring of tissue growth and viability in 3D tissue-engineering
347 scaffolds, *J. Tissue Eng. Regen. Med.* 9(5), 641-645(2015)

348 [31] P.O. Bagnaninchi, C. Holmes, N. Drummond, J. Daoud, M. Tabrizian, Two-dimensional and three-
349 dimensional viability measurements of adult stem cells with optical coherence phase microscopy, *J.*
350 *Biomed. Opt.* 16(8), 086003(2011)

351 [32] L. A. G. Lin, A. Q. Liu, Y. F. Yu, C. Zhang, C. S. Lim, S. H. Ng, P. H. Yap, H. J. Gao, Cell
352 compressibility studies utilizing noncontact hydrostatic pressure measurements on single living cells
353 in a microchamber, *Appl. Phys. Lett.* 92(23), 233901(2008)

- 354 [33] K. S. Lee, H. Hur, H. Y. Sung, I. J. Kim, G. H. Kim, Spectrally encoded common-path fiber-optic-
355 based parallel optical coherence tomography, *Opt. Lett.* 41(18), 4241-4244(2016)
- 356 **[34] Pierre phase stability [Bagnaninchi P, *Journal biomedical optics*, 2011]**
- 357 [35] M. V. Sarunic, B. E. Applegate, J. A. Izatt, Real-time quadrature projection complex conjugate
358 resolved Fourier domain optical coherence tomography, *Opt. Lett.* 31(16), 2426-2428(2006)
- 359 [36] K. Kim, J. Cheung, Q. Liu, X. Y. Wu, Y. Sun, Investigation of mechanical properties of soft
360 hydrogel microcapsules in relation to protein delivery using a MEMS force sensor, *J. Biomed. Mater.*
361 *Res.* 92(1), 103-113(2010)
- 362 [37] W. J. Ellridge, A. Sheinfeld, M. T. Rinehart, A. Wax, Imaging deformation of adherent cells due
363 to shear stress using quantitative phase imaging, *Opt. Lett.* 41(2), 352-355(2016)
- 364 [38] Y. M. Efremov, W. Wang, S. D. Hardy, R. L. Geahlen, A. Raman, Measuring nanoscale viscoelastic
365 parameters of cells directly from AFM force-displacement curves, *Sci. Rep.* 7, 1541(2017)
- 366 [39] <https://link.springer.com/article/10.1186/s40644-016-0070-8>
- 367 [40] <https://www.ncbi.nlm.nih.gov/pmc/articles/PMC5108442/>
- 368 [41] <http://www.sciencedirect.com/science/article/pii/S0720048X15000248#!>
- 369 [42] <https://link.springer.com/article/10.1007/s12020-015-0654-2>
- 370 [43] <http://rsif.royalsocietypublishing.org/content/8/64/1521>
- 371 [44] <http://iopscience.iop.org/article/10.1088/0031-9155/58/4/923/meta>



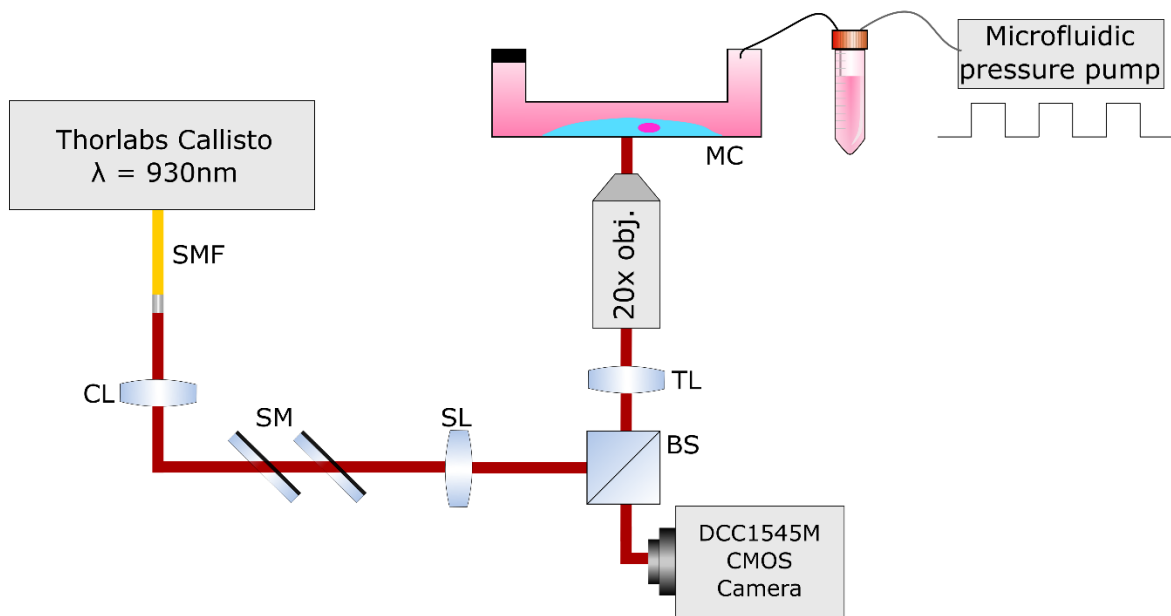
372

373

Figure 1: Resulting hydrostatic force induced on adherent cells above a substrate

374

375



376

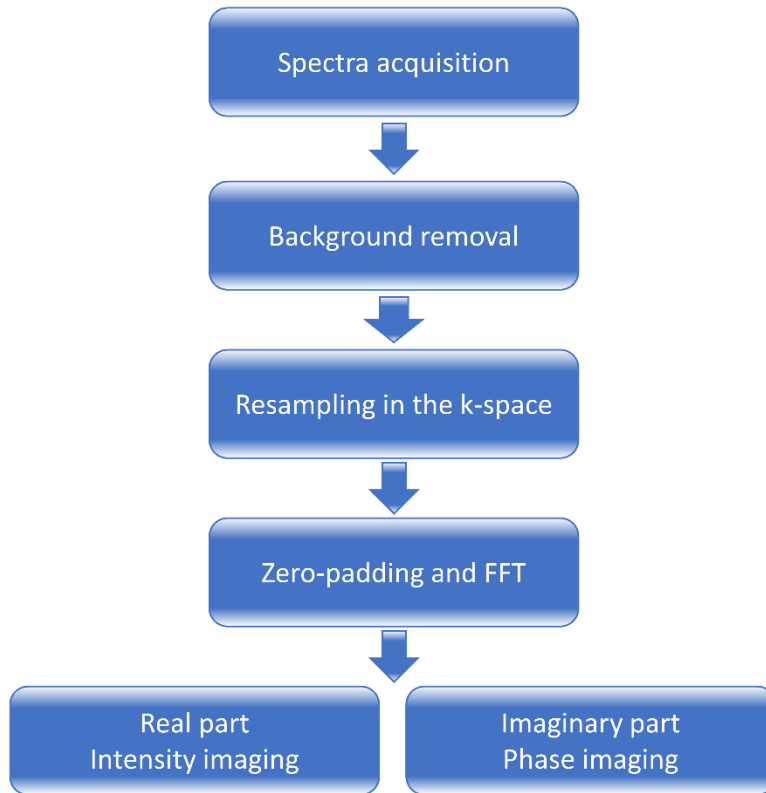
377

378

379

Figure 2: OCPM set-up for qualitative measurement of cell mechanical properties: SMF, single mode fibre; CL, collimating lens; SM, scanning mirrors; SL, scanning lens; BS, beam splitter; TL, tube lens; MC, microchannel.

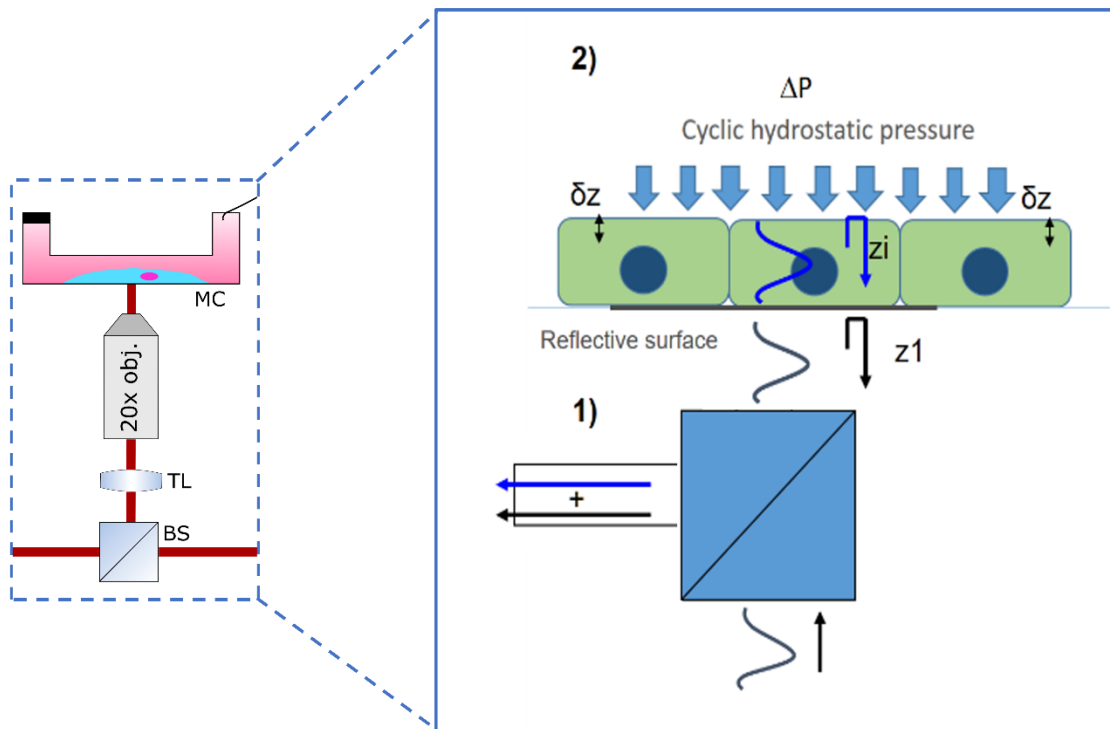
380



381

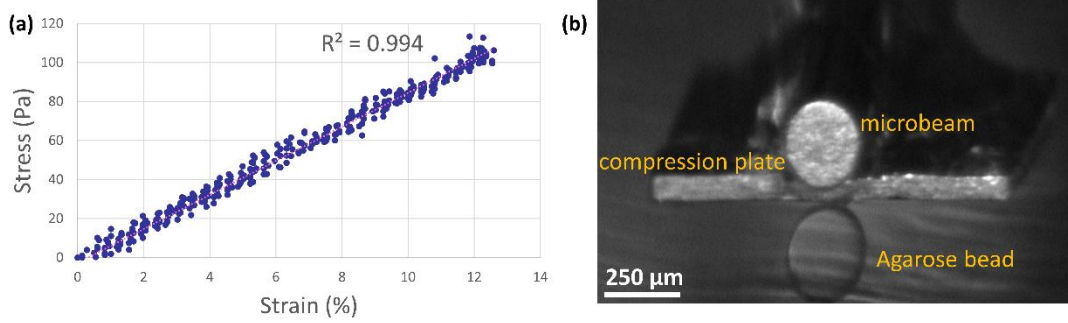
382 *Figure 3: Digital processing of acquired OCPM spectra to retrieve intensity image and phase information at each pixel.*

383



384

385 *Figure 4: Relative displacement induced by hydrostatic pressure measured as a change in phase. 1) Imaging system 2) Cyclic*
 386 *hydrostatic pressure is applied to cells which are cultured on a clear, reflective surface, which results in a change in the*
 387 *phase signal.*

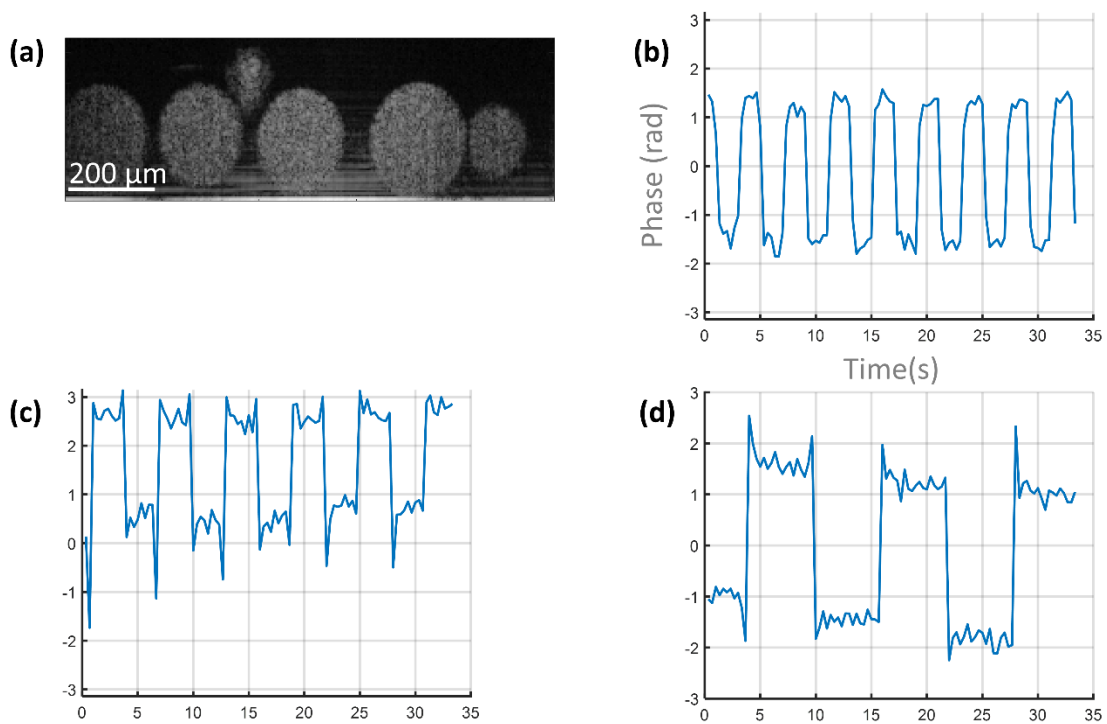


388

389

390

Figure 5: Mechanical properties of 6% agarose beads: Representative stress-strain curve of 350 μm bead (a), and compression testing in a water bath at strain rate of 2.5 μm/s (b).

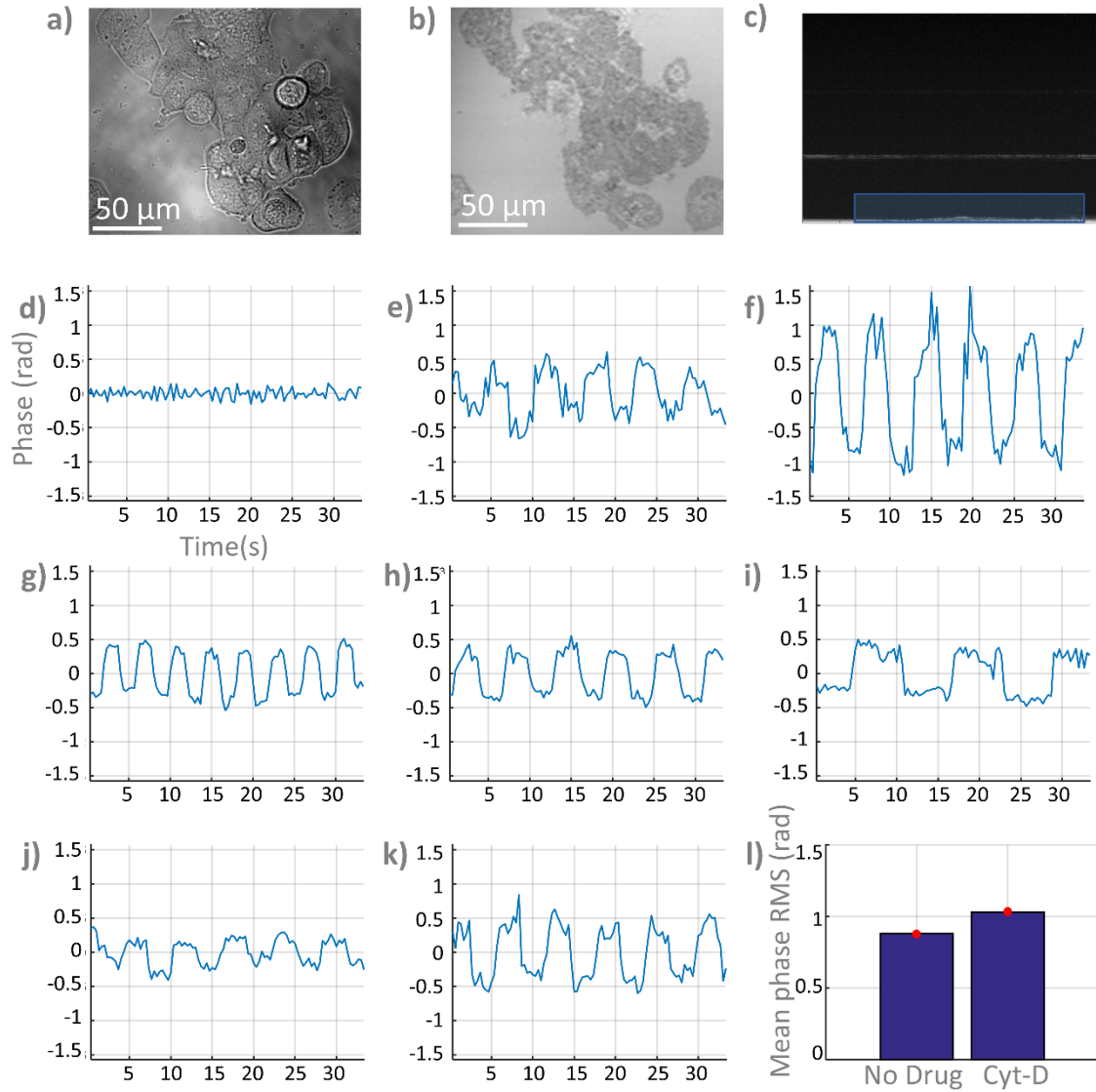


391

392

393

Figure 6: a) OCPM cross section of agarose beads, b-d) response to hydrostatic pressure of 4 s, 6 s, 12 s cycles with 100 mbar amplitude.



394

395

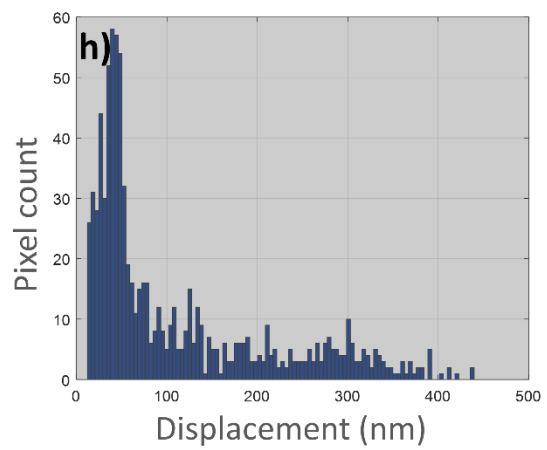
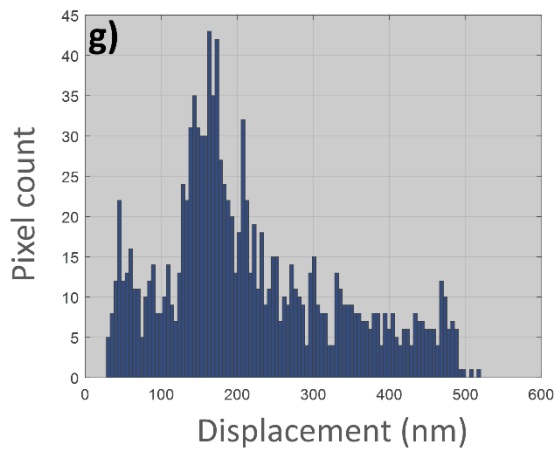
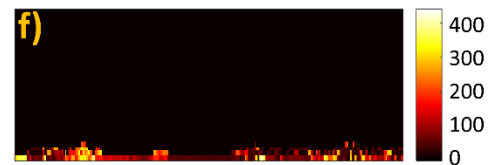
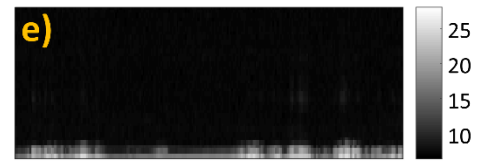
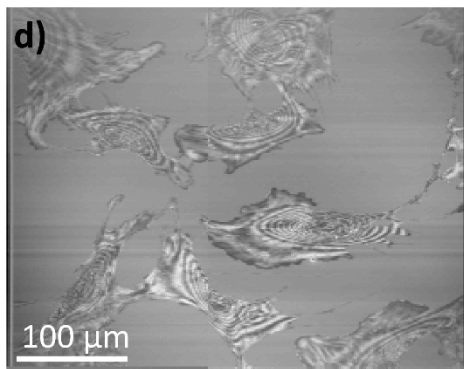
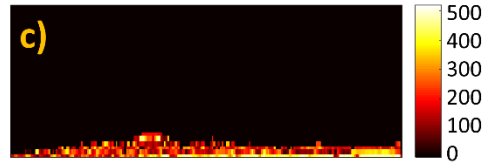
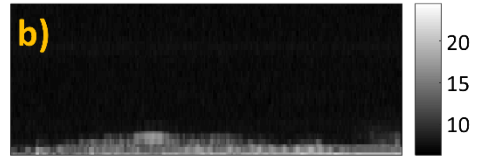
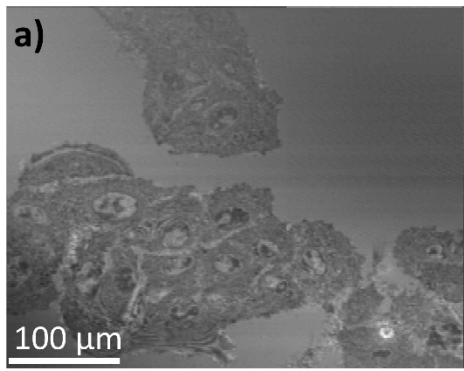
396

397

398

399

Figure 7: Bright field image (a), OCPM en-face (b), and OCPM 'cell profile' (c) of MCF-7 cells. Cell response at 0, 100, 200 mbar amplitude (d, e, f) with a 6 s cycle, and for various hydrostatic pressure period, 4 s, 6 s, 12 s cycles with 200 mbar amplitude (g, h, i), and (j) Typical cell response before drug addition (6 s, 50 mbar) and after addition of 10 μ M Cytochalasin-D (k). (l) Mean response (N=242 pixels) shows significant ($p < 0.01$) increase in cell response. Phase value was taken at a representative pixel rather than the same pixel location within the cell.



400

401

402

403

404

405

Figure 8: OCPM en-face live imaging of MCF-7 cells (a) and 3T3 cells (d) with typical OCPM cross-section, 'cell profile', (b) and (e) and associated relative cell displacement induced by hydrostatic pressure (c) and (f). Heterogeneity in intracellular displacement was found in histograms of displacement (g, h) with a marked difference between 3T3 and MCF-7 which suggested 3T3 being stiffer.